machines

MDPI

Article

Discrete Element Modelling Method and Parameter Calibration of Mussel Based on Bonding V2 Model

Zhenhua Li [1], Xinyang Li [1], Chen Li [2] and Hongbao Ye [2,3,*]

[1] School of Marine Engineering Equipment, Zhejiang Ocean University, Zhoushan 316022, China; lizh760905@zjou.edu.cn (Z.L.)
[2] Zhejiang Academy of Agricultural Sciences, Hangzhou 310058, China
[3] Key Laboratory of Agricultural Equipment for Hilly and Mountainous Areas in Southeastern China (Co-Construction by Ministry and Province), Ministry of Agriculture and Rural Affairs, Hangzhou 310058, China
* Correspondence: yehb.zaas@gmail.com

Abstract

To address the inefficiency and high labor intensity associated with traditional manual mussel seedling unloading, this study proposes an automated traction-rope mussel unloading machine. This study focuses on the thick-shelled mussel (*Mytilus coruscus*) as the research subject. Furthermore, the key mussel unloading processes were simulated using the EDEM software to analyze mechanical interactions during detachment. A breakable mussel discrete element model was developed, and its Bonding V2 model parameters were systematically calibrated. Using the ultimate crushing displacement (2.25 mm) and ultimate crushing load (552 N) as response variables, the model was optimized through a sequential experimental design comprising Plackett–Burman screening, the steepest ascent method, and the Box–Behnken response surface methodology. The results demonstrate that the optimal parameter combination consists of unit area normal stiffness (2.48×10^{11} N/m^3), unit area tangential stiffness (3.80×10^8 N/m^3), critical normal stress (3.15×10^6 Pa), critical tangential stress (2.90×10^7 Pa), and the contact radius (1.60 mm). The model's accuracy was validated through integrated discrete element simulations and prototype testing. The equipment achieves an exceptionally low mussel damage rate of only 1.2%, effectively meeting the operational requirements for mussel unloading. This study provides both theoretical foundations and practical insights for the design of mechanized mussel unloading systems in China.

Keywords: mytilus crassitesta; automatic unloading seedlings; bonding V2; parameter calibration

Check for updates

Academic Editor: Yucheng Liu

Received: 23 December 2025
Revised: 5 January 2026
Accepted: 8 January 2026
Published: 10 January 2026

Copyright: © 2026 by the authors. Licensee MDPI, Basel, Switzerland. This article is an open access article distributed under the terms and conditions of the Creative Commons Attribution (CC BY) license.

1. Introduction

Mussels (*Mytilus* spp.) are among the most economically significant shellfish species in China, with a cultivation area of approximately 44,000 hectares and an annual production of ~890,000 tons, representing nearly 40% of the global output [1]. Currently, the mussel industry is undergoing a transformative shift from traditional aquaculture practices to modern high-quality development. However, several bottlenecks hinder its progress, particularly in breeding techniques. For instance, the conventional segmented artificial seedling unloading method can no longer meet the demands of efficient and intensive industrial development. The mussel breeding industry faces several critical challenges, including high labor intensity, low unloading efficiency, and elevated seedling damage rates. These issues significantly hinder the sustainable development and large-scale expansion

of the sector [2]. Therefore, developing an automated mussel unloading machine with high efficiency and superior performance is crucial for advancing the mechanization of the mussel breeding industry.

In the field of mussel unloading devices, extensive research has been conducted by scholars worldwide. Notably, studies on pretreatment technologies for major economic shellfish species were initiated earlier in foreign countries, where the processes have now reached maturity with well-established workflows and management systems [3,4]. On the west coast of France, fishermen employ a stake-based mussel farming system. Upon maturation, the mussels are harvested using a vertical sleeve-type machine, which envelops the entire stake from top to bottom. Subsequently, a locking mechanism secures the peeling disc, enabling the device to ascend and detach the mussels through a controlled scraping action. In New Zealand, mussel farming predominantly utilizes raft-based cultivation systems. During harvesting, vessels are equipped with integrated mechanical pipelines to facilitate simultaneous collection and cleaning. The separation process employs specialized mussel separators, which detach mussels from culture ropes through mechanical action (e.g., rotating drums or brushes) or hydrodynamic methods (e.g., high-pressure water jets) [5]. In China, Luo et al. [6] proposed a mechanized mussel harvesting device with integrated automatic picking and classification functions. The core component of this system is a threshing brush mechanism. During operation, the culture rope is guided through the rotating threshing brush, which efficiently detaches mussels through mechanical action. In 2019, Cheng et al. [7] developed a chain-type mussel unloading device, where unloading hooks were mounted on the links of a transmission chain. The periodic motion of the chain drives the seedling rope forward, guiding it between two counter-rotating threshing cylinders. Through this mechanism, the mussels are effectively detached via mechanical scraping. In 2021, Cheng et al. [8] developed a screw-driven mussel unloading system, incorporating PLC-based automatic control as a key enhancement over conventional unloading devices.

In summary, shellfish pretreatment and processing technologies have been well-established and widely adopted in developed countries, including those in Europe, North America, and Japan. However, due to regional variations in aquaculture practices, specialized equipment from these regions cannot be directly applied in China without necessary modifications to accommodate local conditions. Currently, research on mussel unloading machines in China remains in the early developmental stage, with most existing equipment limited to laboratory or pilot-scale applications. Despite the gradual adoption of mechanized tools by frontline fishermen, manual harvesting and cleaning processes still dominate practical operations [9]. To address these challenges, this study focuses on mussels from Shengsi Island, Zhejiang Province, and proposes an automated traction-rope mussel unloading machine. Utilizing the Discrete Element Method (DEM) simulation, we conducted peeling tests and developed a functional prototype for experimental validation. The critical structural and operational parameters of the mussel unloading machine were systematically determined, providing a theoretical foundation and practical guidance for the widespread adoption of mechanized mussel harvesting technology.

2. Overall Structure and Working Principle

2.1. Overall Structure

The mussel automatic traction-rope unloading seedling machine is composed of an unloading seedling mechanism and a traction winding mechanism. The seedling unloading mechanism includes a conveying channel, a seedling unloading disc, a V-shaped guide frame, a hopper and a frame; The traction winding mechanism set in the downstream of the seedling unloading mechanism includes a support frame, a rope winding unit and a

rope unloading unit. The structure of the whole machine is shown in Figure 1, and the main technical parameters are shown in Table 1.

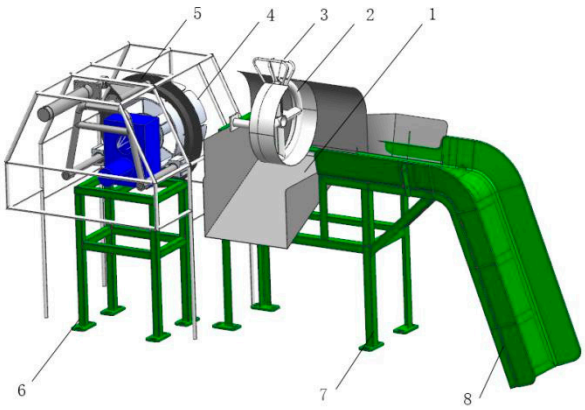


Figure 1. An Automatic Traction and Rope-retracting Mussel Seed-unloading Device. 1. Hopper; 2. Seedling unloading disc; 3. V-shaped guide frame; 4. Rope winding unit; 5. Rope unloading unit; 6. Support frame; 7. Frame; 8. Conveying channel.

Table 1. Main technical parameters.

Parameter	Value
length × width × height	2800 mm × 1115 mm × 1500 mm
Number of jobs/cluster	1
Operating speed/t·h^{-1}	8–10
matching power/kW	7.5

2.2. Working Principle

After the mussel string is salvaged out of the sea, the operator hangs the hanging rope of the breeding rope to the hook of the extension rope, and the rope winding unit starts to act. The driving device drives the winding part to rotate, and the winding part drives the extension rope to make the mussel string along the conveying channel. It is sent to the vicinity of the unloading disc; During the conveying process, due to the smooth transition between the slope section and the horizontal section, the extension rope can still drive the mussels to enter serially at the transition between the two. When the breeding rope moves above the V-shaped guiding component, it can enter the unloading hole in the center of the unloading disc along the guiding channel under the action of the V-shaped guiding component. Because the size of the unloading hole is similar to the diameter of the breeding rope, the mussels will be peeled off from the breeding rope by dragging in the process of the breeding rope approaching the traction winding mechanism through the unloading hole. The breeding rope is wound on the outer reel with the extension rope. When the photoelectric switch detects that there is no rope between the winding part and the unloading disc, the whole mussel string is unloaded. Then the controller sends instructions to the traction winding mechanism, the rope winding unit stops and the rope unloading unit starts to run. The driving mechanism drives the annular push plate to push the breeding rope coiled on the outer drum into the storage basket. The breeding rope is separated from the hook, and then the next mussel string is operated.

3. Discrete Element EDEM Simulation Parameter Calibration

3.1. Selection of the Contact Model

The discrete element method is a numerical simulation method used to study particle motion and mechanical behavior. The particle system is regarded as a set of discrete

elements. The motion state of each particle is discretized, modeled and calculated. The interaction between particles and the overall motion law are studied by numerical simulations [10]. The contact model is used to describe and calculate the mechanical behavior between particles and between particles and boundaries so that particles can simulate actual physical phenomena, such as collision, friction, adhesion and separation. The selection of the contact model and its parameter setting directly affect the accuracy and reliability of the simulation.

In the EDEM software, many contact models are built in, such as Hertz—Mindlin (no slip) [11], Hertz—Mindlin with JKR [12], Bonding V2 [13], etc. Bonding V2 model can be used to analyze the crushing process between particles from a microscopic point of view, which can be used to simulate the damage and bonding behavior of mussels [14]. In this paper, based on the Hertz-Mindlin (no slip) model, Bonding V2 is added as the contact model between particles on the basis of this model. The interaction between mussels during the peeling process of real mussel string is simulated by the viscous connection bond between particles. The two contact principles are as follows:

1. Hertz—Mindlin (no slip) model:

Hertz—Mindlin (no slip) model. It is the core physical model for dealing with particle contact in discrete element method. The contact principle and key formulas are as follows:

The normal force F_n is determined by the amount of particle overlap δ and the elastic properties of the material:

$$F_n = \frac{4}{3} E^* \sqrt{R^*} \delta^{\frac{3}{2}} \tag{1}$$

Among them:

Comprehensive elastic modulus E^*:

$$\frac{1}{E^*} = \frac{1 - {\nu_1}^2}{E_1} + \frac{1 - {\nu_2}^2}{E_2} \tag{2}$$

E_1, E_2—Elastic modulus of two contacting particles, ν_1, ν_2—Poisson's ratio.

Comprehensive radius of curvature R^*:

$$\frac{1}{R^*} = \frac{1}{R_1} + \frac{1}{R_2} \tag{3}$$

R_1, R_2—Contact point radius of curvature.

The tangential force F_t is limited by the no-slip condition:

Tangential force increment:

$$\Delta F_t = -k_t \Delta \delta_t \tag{4}$$

k_t—Tangential stiffness, $\Delta \delta_t$—Tangential displacement increment.

No sliding constraint:

$$|F_t| \leq \mu F_n \tag{5}$$

μ is the static friction coefficient to ensure that the contact point does not slide relatively.

The normal and tangential damping forces introduce velocity—dependent dissipation terms:

$$F_{damp,n} = -c_n v_n, F_{damp,t} = -c_t v_t \tag{6}$$

The damping coefficients c_n and c_t are associated with the recovery coefficient to simulate the collision energy loss.

2. Bonding V2 model:

Bonding V2 model is a contact model for simulating the mechanical behavior of viscous or flexible materials in the discrete element method. The core principle is to connect the

particle element through the virtual bond, and simulate the bonding, plastic deformation and fracture process of the material through the mechanical response of the bond. The contact principle and key formulas are as follows:

Normal force F_n and tangential force F_t:

The normal force is calculated by overlap δ_n and normal stiffness k_n:

$$F_n = k_n \cdot A \cdot \delta_n \tag{7}$$

Tangential force is calculated by tangential displacement δ_t and tangential stiffness k_t:

$$F_t = k_t \cdot A \cdot \delta_t \tag{8}$$

where A is the equivalent cross-sectional area of the bond.

k_n—Normal stiffness per unit area, N/m^3, control the normal deformation resistance.

k_t—Tangential stiffness per unit area, N/m^3, control the tangential deformation resistance.

The viscoelastic damping term is introduced to simulate the energy dissipation in the yield stage:

$$F_{damp} = -c \cdot v \tag{9}$$

The damping coefficient is optimized by central composite design (CCD) to match the data on the yield resistance test of the material.

3.2. Parameter Determination Test

3.2.1. Uniaxial Compression Test

Mytilus crassitesta in Shengsi, Zhoushan, Zhejiang Province, was taken as the research object. In order to construct an accurate mussel particle model, mussel shells with complete and no obvious damage were selected for a uniaxial compression test by a universal tester, as shown in Figure 2.



Figure 2. Universal tester.

The prepared mussel shell is placed in the center of the loading platform of the universal testing machine to ensure that the specimen is concentric with the loading head and avoid the deviation of the test results caused by eccentric loading. At a loading rate of 0.1 mm/min, the axial pressure is applied to the specimen slowly and uniformly. When the mussel shell shows obvious signs of damage, such as the rapid expansion of cracks, the sudden change in sound, and the load no longer increases but decreases, it is determined that the specimen has reached the failure state. At this time, the loading is stopped and the test is completed. The load–displacement curve is drawn, as shown in Figure 3, which intuitively shows the mechanical response characteristics of mussel shells during uniaxial compression [15]. It can be seen from the figure that the ultimate bearing load of mussel shell is about 552 N.

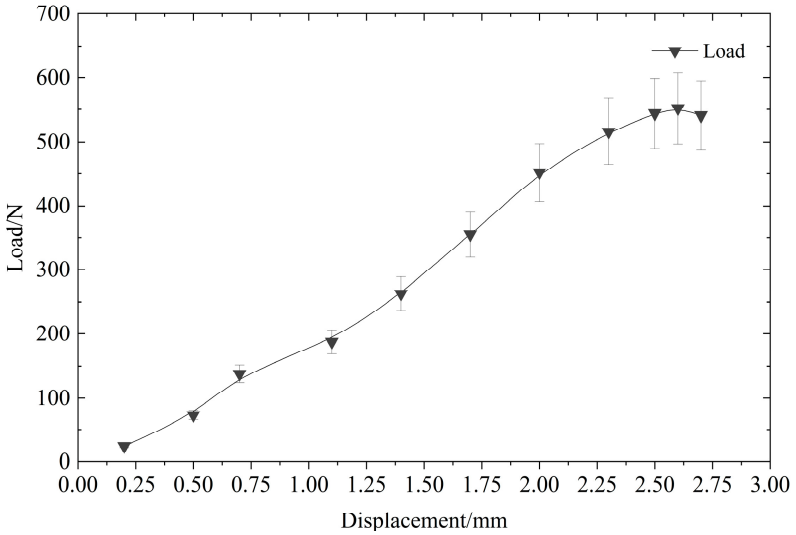


Figure 3. Load—displacement curve.

3.2.2. Mussel Byssus Bonding Characteristic Test

The mussel realizes the adhesion between individuals through foot protein. The establishment of the mussel string particle model requires the support of the mussel byssus adhesion strength data [16]. The experimental model is shown in Figure 4. The tension meter is fixed on the horizontal frame, and the tension end is installed with a fixture to clamp the connection belt. The connection belt fixes one side of the mussel, and the other side of the mussel is connected with the rocker end fixture. The mussels were fixed and the tension meter moved until the mussel byssus was broken.

The concentration ranges of shell length, shell width and shell thickness are 101–110 mm, 41–50 mm and 31–40 mm. The experiment was divided into three groups: the first group, single mussel and single mussel; the second group, single mussel and multiple mussels; the third group, multiple mussels and multiple mussels. In order to eliminate the contingency during the experiment, each group was subjected to 10 identical tests, and unbroken mussels with different compositions were selected as experimental subjects. The experimental results are shown in Table 2. According to the measurement results, the maximum tensile force of mussel byssus fracture between single mussels is 58.74 N, the maximum tensile force of mussel byssus fracture between single mussels and multiple mussels is 78.89 N, and the maximum tensile force of mussel byssus fracture between multiple mussels is 215.60 N.

Table 2. Mechanical test results of byssus.

Serial Number	Pulling Force	Maximum	Serial Number	Pulling Force	Maximum	Serial Number	Pulling Force	Maximum
1-1	56.73	58.74	2-1	78.89	78.89	3-1	215.60	215.60
1-2	49.00		2-2	73.50		3-2	214.13	
1-3	27.44		2-3	69.58		3-3	179.83	
1-4	29.89		2-4	57.82		3-4	160.23	
1-5	24.99		2-5	55.87		3-5	142.59	
1-6	52.92		2-6	53.90		3-6	101.43	
1-7	46.55		2-7	53.41		3-7	98.98	
1-8	35.62		2-8	50.74		3-8	98.00	
1-9	58.74		2-9	46.06		3-9	95.55	
1-10	46.51		2-10	38.22		3-10	63.70	



Figure 4. Experiment on the Adhesive Strength of Mussel byssus.

3.3. Uniaxial Compression Simulation Test

3.3.1. Uniaxial Compression Simulation Test Process

The outer surface of the mussel is irregularly curved. The model establishment process in EDEM is complicated. A large number of particles are needed to fill the model, and the particles need to form bonding bonds [17]. Therefore, according to the morphological distribution of mussels, Solid Works software was used for three- dimensional modeling. After the material property parameters are set, multi-spherical particles are added to 'Beike' and imported into Solid Works to complete and save the mussel model in STL format, as shown in Figure 5a. After the completion of the import, the rapid filling is carried out, which is composed of 53 spherical particles and the radius is not unique, as shown in Figure 5b.



(**a**) Mussel three-dimensional model (**b**) Mussel particle model

Figure 5. Model of mussels.

The seedling rope particle model is modeled by manually adding particles. In order to simplify the calculation and facilitate the adhesion of mussels, the seedling rope model is simplified into a simple cylindrical model with spherical particles arranged horizontally, and it is is composed of 123 spherical particles, as shown in Figure 6.



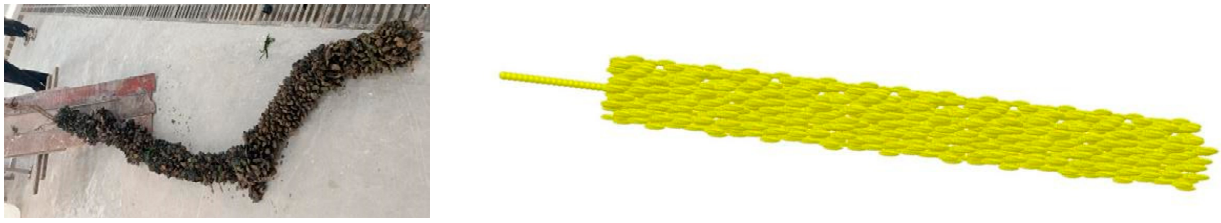
(**a**) The object of seedling rope (**b**) Particle model of seedling rope

Figure 6. Model of the mussel seedling rope.

The particle radius is set to 20 mm, and the contact radius of the particles is set to 26 mm. When the distance between particles is less than the contact radius, there will be a bonding effect between particles [18].

The discrete element modeling of mussel string belongs to composite particle modeling. 'Meta-Particle' allows the combination of multiple basic particles into complex structures, and realizes the simulation of real material morphology through hierarchical nesting,

which can simulate the release behavior of sub-particles during particle breakage [19]. By manually adding particle coordinates, mussel particles are arranged on the seedling rope, and finally a mussel string particle model with a length of 3000 mm (including the length of the front-end traction rope) and a diameter of about 30 mm is formed, as shown in Figure 7.



(**a**) The object of mussel string (**b**) Particle model of mussel string

Figure 7. Model of cultivated mussel strings.

3.3.2. Simulation Test Process of Uniaxial Compression

The compression test was carried out by using the discrete element simulation software EDEM 2023, and the extrusion condition of mussels on the universal tester was simulated, as shown in Figure 8.

The basic physical parameters of mussels used in the simulation, the contact parameters between mussels and seedling ropes, and between mussels and equipment are obtained according to pre-tests and literature [20–23], as shown in Table 3.

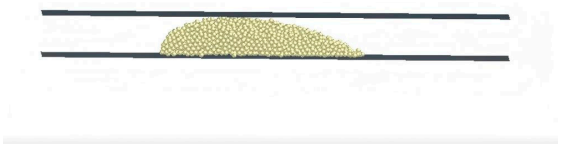
Table 3. Physical characteristic parameters of material.

Material	Parameters	Value
Mussel shell	Poisson's ratio	0.394
	Density (kg/m^3)	1580
	Shear modulus (Pa)	5.56×10^7
Seeding rope	Poisson's ratio	0.33
	Density (kg/m^3)	930
	Shear modulus (Pa)	2.9×10^9
Equipment	Poisson's ratio	0.29
	Density (kg/m^3)	7930
	Shear modulus (Pa)	1.93×10^{11}
Mussel-Mussel	Restitution coefficient	0.32
	Static friction coefficient	1.25
	Rolling friction coefficient	0.33
Mussel-Seeding rope	Restitution coefficient	0.1
	Static friction coefficient	0.1
	Rolling friction coefficient	0.3
The mussel string-Equipment	Restitution coefficient	0.38
	Static friction coefficient	0.23
	Rolling friction coefficient	0.34

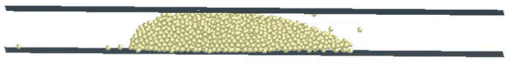
3.4. Parameter Calibration of Bonding V2 Model

As a well-studied biomineral composite, the mussel shell exhibits a unique combination of biogenic minerals and organic matrices, making it a model system for biomimetic material design. The ultimate crushing load corresponds to the maximum destructive force tolerable by mussels during predation or environmental disturbances, providing a quantitative measure of their 'defense level'. Ultimate crushing displacement represents the deformation energy absorption capacity of the shell before catastrophic failure,

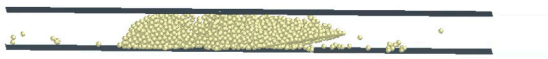
providing a key metric for assessing its structural robustness under destructive loads. Increased crushing displacement corresponds to enhanced toughness, whereby the material dissipates impact energy through large plastic deformation, avoiding sudden brittle fracture. Calibration enables the discrete element method (DEM) model to serve as a robust tool for bionic engineering design. Thus, this section focuses on mussels' ultimate load and ultimate displacement to inversely determine the optimal material composition and processing parameters.



(**a**) Initial state



(**b**) Critical state



(**c**) Crash state

Figure 8. Uniaxial compression simulation test.

3.4.1. Plackett–Burman Design

The five factors of this test are the normal stiffness per unit area X_1, the tangential stiffness per unit area X_2, the critical normal stress X_3, the critical tangential stress X_4 and the contact radius X_5. Taking the ultimate crushing displacement Y_1 and the ultimate crushing load Y_2 as the response, the range of each parameter is obtained from the literature and the upper and lower range values are determined [24,25]. The test factor levels are shown in Table 4.

The results of the Plackett—Burman design are shown in Table 5. In order to obtain the significant effect of each factor, the Design-Expert was used for variance analysis and *t*-test to select the significant factors. The results are shown in Table 6 and Figure 9, respectively.

Table 4. Plackett—Burman test factor levels.

Factors	Coding	
	−1	**1**
Normal stiffness per unit area X_1/N·m^{-3}	2.00×10^{11}	2.80×10^{11}
Tangential stiffness per unit area X_2/N·m^{-3}	3.20×10^{8}	4.40×10^{8}
Critical normal stress X_3/Pa	2.80×10^{6}	3.50×10^{6}
Critical tangential stress X_4/Pa	1.90×10^{7}	2.30×10^{7}
Radius of contact X_5/mm	1.60	2.40

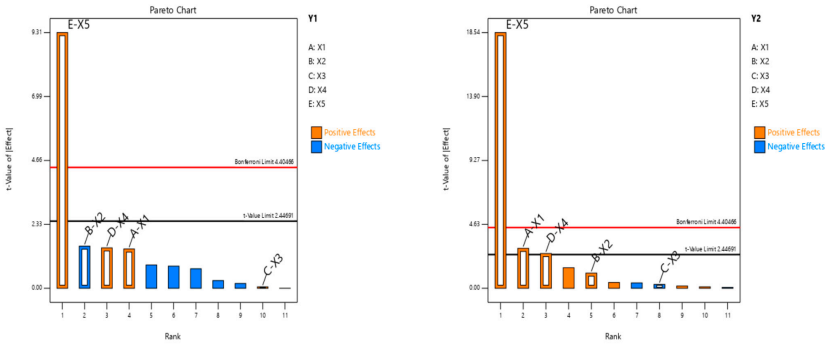
Table 5. Plackett—Burman test results.

Serial Number	Factors					Response Value	
	$X_1/(N \cdot m^{-3})$	$X_2/(N \cdot m^{-3})$	X_3/Pa	X_4/Pa	X_5/mm	Y_1/mm	Y_2/N
1	2.80×10^{11}	3.20×10^{8}	3.50×10^{6}	2.30×10^{7}	1.60	1.975	350.706
2	2.80×10^{11}	3.20×10^{8}	2.80×10^{6}	1.90×10^{7}	2.40	2.605	804.722
3	2.00×10^{11}	3.20×10^{8}	2.80×10^{6}	2.30×10^{7}	1.60	1.775	293.962
4	2.80×10^{11}	4.40×10^{8}	3.50×10^{6}	1.90×10^{7}	1.60	1.740	372.789
5	2.80×10^{11}	4.40×10^{8}	2.80×10^{6}	1.90×10^{7}	1.60	1.740	372.789
6	2.00×10^{11}	4.40×10^{8}	3.50×10^{6}	1.90×10^{7}	2.40	2.140	707.576
7	2.00×10^{11}	4.40×10^{8}	3.50×10^{6}	2.30×10^{7}	1.60	1.815	380.175
8	2.80×10^{11}	3.20×10^{8}	3.50×10^{6}	2.30×10^{7}	2.40	2.650	915.249
9	2.00×10^{11}	4.40×10^{8}	2.80×10^{6}	2.30×10^{7}	2.40	2.375	863.556
10	2.00×10^{11}	3.20×10^{8}	2.80×10^{6}	1.90×10^{7}	1.60	1.785	296.200
11	2.00×10^{11}	3.20×10^{8}	3.50×10^{6}	1.90×10^{7}	2.40	2.420	748.194
12	2.80×10^{11}	4.40×10^{8}	2.80×10^{6}	2.30×10^{7}	2.40	2.440	887.210

Table 6. Variance analysis of Plackett—Burman.

Source	Y_1/mm					Y_2/N				
	Sum of Squares	df	Mean Square	F-Value	*p*-Value	Sum of Squares	df	Mean Square	F-Value	*p*-Value
Model	1.32	5	0.2650	19.10	0.0013 *	7.11×10^{5}	5	1.422×10^{5}	71.69	<0.0001 *
X_1	0.0284	1	0.0284	2.04	0.2027	16,624.04	1	16,624.04	8.38	0.0275 *
X_2	0.0326	1	0.0326	2.35	0.1759	2394.58	1	2394.58	1.21	0.3140
X_3	0.0002	1	0.0002	0.0024	0.9625	159.51	1	159.51	0.0804	0.7863
X_4	0.0300	1	0.0300	2.16	0.1918	12,583.3	1	12,583.30	6.34	0.0454 *
X_5	1.20	1	1.20	86.76	<0.0001 *	6.816×10^{5}	1	6.816×10^{5}	343.65	<0.0001 *
Residual	0.0832	6	0.0139			11,900.22	6	1983.37		

Note: * indicates significant difference. ($p < 0.05$).



(**a**) the ultimate crushing displacement (**b**) the ultimate crushing load

Figure 9. Pareto chart.

Through Table 6 and Figure 9, it can be seen that the order of influence on the ultimate crushing displacement Y_1 is X_5, X_2, X_4, X_1, X_3, and the influencing factor X_5 is significant and positive. The order of influence on the ultimate crushing load Y_2 is X_5, X_1, X_4, X_2, X_3, and the influencing factors X_1, X_4, X_5 represent significant and positive effects.

The regression equation of each factor on the ultimate crushing displacement Y_1 and the ultimate crushing load Y_2 is

$$Y_1 = 2.12 + 0.0516X_1 - 0.0553X_2 + 0.0017X_3 + 0.0500X_4 + 0.3167X_5 \quad (10)$$

$$Y_2 = 582.76 + 39.48X_1 + 14.98X_2 - 3.65X_3 + 32.38X_4 + 238.32X_5 \quad (11)$$

3.4.2. Steepest Ascent Test

According to the results of the Plackett–Burman test, X_2 and X_3 had no significant effect on the target value, so X_2 was 3.80×10^8 N/m^3 and X_3 was $3.153.15 \times 10^6$ Pa. The initial values of X_1, X_4 and X_5 were selected as 2.00×10^{11} N/m^3, 1.90×10^7 Pa and 1.6 mm, and the step sizes of X_1, X_4 and X_5 were determined as 1.60×10^{10} N/m^3, 2.00×10^6 Pa and 0.2 mm. The Steepest ascent test was carried out to obtain the parameter combination closest to the real value. The test scheme and results are shown in Table 7.

Table 7. Steepest ascent test program and results.

Serial Number	Factors			Y_1/mm	Y_2/N
	X_1/(N·m^{-3})	X_4/Pa	X_5/mm		
1	2.00×10^{11}	1.90×10^7	1.60	2.824	460.959
2	2.16×10^{11}	2.10×10^8	1.80	1.723	602.229
3	2.32×10^{11}	2.30×10^8	2.00	1.771	589.149
4	2.48×10^{11}	2.50×10^8	2.20	1.819	576.591
5	2.64×10^{11}	2.70×10^8	2.40	2.154	535.780
6	2.80×10^{11}	2.90×10^8	2.60	2.633	471.947

According to the preliminary test, the ultimate crushing displacement and ultimate crushing load of mussels are 2.250 mm and 552 N. It can be seen from Table 7 that the error between the ultimate crushing displacement, load and the real value decreases first and then increases, and the error between the fifth group of test results and the real value is the smallest.

3.4.3. Box–Behnken Test

According to the results of the Steepest ascent test, the Box–Behnken test was carried out with the parameter combinations of tests 4, 5, and 6 as low, medium, and high levels. The test factor levels are shown in Table 8.

Table 8. Box—Behnken test factor levels.

Coding	X_1/(N·m^{-3})	X_4/Pa	X_5/mm
−1	2.48×10^{11}	2.50×10^8	2.20
0	2.64×10^{11}	2.70×10^8	2.40
1	2.80×10^{11}	2.90×10^8	2.60

The test plan and results are shown in Table 9, and the results of variance analysis are shown in Table 10.

It can be seen from Table 10 that the quadratic regression model of response values Y_1 and Y_2 has $p = 0.0002 < 0.05$, $p = 0.0028 < 0.05$, $R^2 = 0.9298 > 0.9$, $R^2 = 0.96699 > 0.9$, indicating that the model has high accuracy.

The steeper the slope of the response surface, the more significant the influence of this factor on the response value. The interaction effects of X_1, X_4 and X_5 on Y_1 and Y_2 are shown in Figure 10, and the results are consistent with the analysis results of the interaction term's p-value in Table 10.

Response surface and contour mapping based on multivariate interactions demonstrated that: under fixed $X_5 = 1$, the contour topology reveals that Y_1 is primarily governed by X_4, as evidenced by the pronounced alignment of isoresponse lines along the X_4 direction. Y_1 exhibits a strong positive response to increasing X_4, reflecting its dominant role in the system. The contour lines are oriented at an angle to the X_1–X_4 plane, suggesting a weak interaction effect between X_1 and X_4. Under $X_4 = -1$, the contour topology reveals that Y_1

is predominantly governed by X_5, as reflected by the pronounced alignment of isoresponse lines along the X_5 direction. As X_5 increases, Y_1 increases. With X_1 held constant at 0, Y_1 is primarily driven by X_4 and X_5, indicating their dominant main effects. With X_1 held constant at 0, the contour topology reveals that Y_1 is governed primarily by X_4 and X_5, with X_4 exerting the strongest influence. A pronounced interaction between X_4 and X_5 is evident from the curvature of isoresponse lines, while X_1 exerts only a secondary, conditional influence. Hierarchical dominance: $X_4 > X_5 > X_1$ [26].

Table 9. Box—Behnken test protocol and results.

Serial Number	Factors			Response Value	
	$X_1/(N \cdot m^{-3})$	$X_4/(N \cdot m^{-3})$	X_5/mm	Y_1/mm	Y_2/N
1	2.64×10^{11}	2.70×10^{8}	2.40	2.130	540.594
2	2.64×10^{11}	2.70×10^{8}	2.40	2.250	551.477
3	2.48×10^{11}	2.70×10^{8}	2.20	2.566	377.296
4	2.80×10^{11}	2.70×10^{8}	2.60	1.838	567.383
5	2.80×10^{11}	2.50×10^{8}	2.40	2.035	543.576
6	2.80×10^{11}	2.90×10^{8}	2.40	2.202	534.106
7	2.48×10^{11}	2.90×10^{8}	2.40	2.010	556.186
8	2.48×10^{11}	2.70×10^{8}	2.60	1.939	561.470
9	2.48×10^{11}	2.50×10^{8}	2.40	2.164	527.670
10	2.64×10^{11}	2.90×10^{8}	2.60	1.987	571.621
11	2.64×10^{11}	2.50×10^{8}	2.60	2.000	574.551
12	2.64×10^{11}	2.70×10^{8}	2.40	2.116	537.036
13	2.64×10^{11}	2.70×10^{8}	2.40	2.106	536.565
14	2.64×10^{11}	2.50×10^{8}	2.20	2.523	475.034
15	2.64×10^{11}	2.70×10^{8}	2.40	2.106	512.600
16	2.80×10^{11}	2.70×10^{8}	2.20	2.590	463.052
17	2.64×10^{11}	2.90×10^{8}	2.20	2.566	464.203

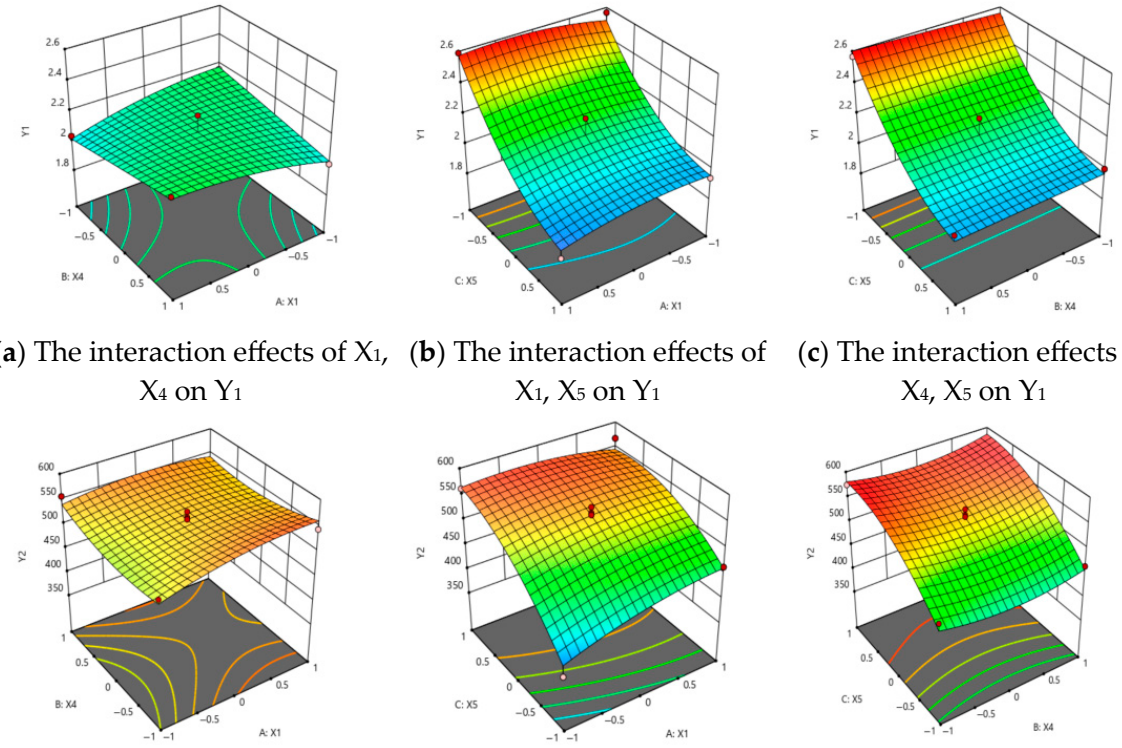
Table 10. Variance analysis of Box—Behnken.

Source	Y_1/mm					Y_2/N				
	Sum of Squares	df	Mean Square	F-Value	*p*-Value	Sum of Squares	df	Mean Square	F-Value	*p*-Value
Model	0.8741	9	0.0971	25.04	0.0002 *	39,359.46	9	4373.27	10.3	0.0028 *
X_1	0.0001	1	0.0001	0.0063	0.9389	913.67	1	913.67	2.15	0.0358 *
X_4	0.0002	1	0.0002	0.0596	0.8142	3.49	1	3.49	0.0082	0.9303
X_5	0.7694	1	0.7694	198.36	<0.0001 *	30,682.60	1	30,682.60	72.27	<0.0001 *
X_1X_4	0.0258	1	0.0258	6.64	0.0366 *	360.73	1	360.73	0.8497	0.3873
X_1X_5	0.0039	1	0.0039	1.01	0.3490	1593.73	1	1593.73	3.75	0.0939
X_4X_5	0.0008	1	0.0008	0.2021	0.6666	15.61	1	15.61	0.0368	0.8534
X_{12}	0.0059	1	0.0059	1.51	0.2588	622.69	1	622.69	1.47	0.2652
X_{42}	0.0000	1	0.0000	0.0026	0.9607	1201.30	1	1201.30	2.83	0.1364
X_{52}	0.0700	1	0.0700	18.05	0.0038 *	4096.91	1	4096.91	9.65	0.0172 *
Residual	0.0272	7	0.0039			2971.90	7	424.56		
Lack of Fit	0.0121	3	0.0040	1.07	0.4563	2162.90	3	720.97	3.56	0.1256

Note: * indicates significant difference. ($p < 0.05$).

With X_5 held constant at 0, contour lines are densely spaced parallel to the X_1 axis, indicating that X_1 exerts a strong influence on Y_2. As X_1 increases, Y_2 increases. With X_4 held constant at 0, contour lines are densely spaced parallel to the X_1 axis, indicating that X_1 dominates the response, while X_5 exerts only a minor influence. Under $X_1 = 0$, the response surface reveals that Y_2 is largely insensitive to changes in X_4 and X_5, as evidenced

by the wide spacing of isoresponse contours. Y_2 is predominantly governed by X_1, with a secondary contribution from X_4 characterized by a marginal interaction, while X_5 exerts negligible influence. This ranking is consistent with the response surface topology [27].



(**a**) The interaction effects of X_1, X_4 on Y_1 (**b**) The interaction effects of X_1, X_5 on Y_1 (**c**) The interaction effects of X_4, X_5 on Y_1

(**d**) The interaction effects of X_1, X_4 on Y_2 (**e**) The interaction effects of X_1, X_5 on Y_2 (**f**) The interaction effects of X_4, X_5 on Y_2

Figure 10. Interaction factor response surface diagram.

The parameter sensitivity comparison is shown in Table 11.

Table 11. Comparison of parameter sensitivity.

Response	Sensitivity Ranking	Key Factor	Secondary Factors	Weak Impact Factor
Y_1	$X_4 > X_5 > X_1$	X_4 (Strong positive correlation)	X_5 (Positive correlation)	X_1
Y_2	$X_1 > X_4 > X_5$	X_1 (Strong positive correlation)	X_4 (Interaction)	X_5

The contour map is shown in Figure 11.

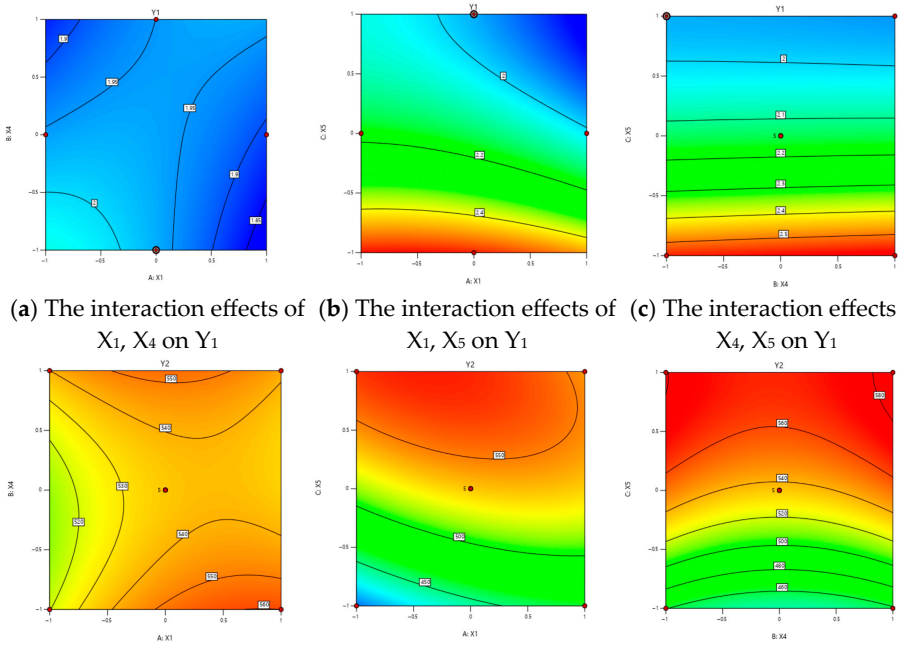
The optimal solution of factors X_1, X_4 and X_5 was analyzed by Design—Expert software. The real values of Y_1 and Y_2 were 2.25 mm and 552 N. Set the constraint condition as:

$$2.48 \times 10^{11}\ \mathrm{N/m^3} \le X_1 \le 2.80 \times 10^{11}\ \mathrm{N/m^3} \quad (12)$$

$$2.50 \times 10^{8}\ \mathrm{N/m^3} \le X_4 \le 2.90 \times 10^{8}\ \mathrm{N/m^3} \quad (13)$$

$$1.60\ \mathrm{mm} \le X_5 \le 2.40\ \mathrm{mm} \quad (14)$$

Finally, X_1, X_4 and X_5 were 2.48×10^{11} N/m^3, 2.90×10^{8} N/m^3 and 1.60 mm, respectively. According to the above experiments, X_2 and X_3 were 3.80×10^{8} N/m^3 and 3.15×10^{6} Pa. As shown in Table 12, this data is the optimal parameter for the simulation test of mature mussel unloading.



(**a**) The interaction effects of X_1, X_4 on Y_1 (**b**) The interaction effects of X_1, X_5 on Y_1 (**c**) The interaction effects of X_4, X_5 on Y_1

(**d**) The interaction effects of X_1, X_4 on Y_2 (**e**) The interaction effects of X_1, X_5 on Y_2 (**f**) The interaction effects of X_4, X_5 on Y_2

Figure 11. Contour map.

Table 12. Bonding V2 model parameters.

Factors	Value
Normal stiffness per unit area X_1/N·m^{-3}	2.48×10^{11}
Tangential stiffness per unit area X_2/N·m^{-3}	3.80×10^{8}
Critical normal stress X_3/Pa	3.15×10^{6}
Critical tangential stress X_4/Pa	2.90×10^{7}
Radius of contact X_5/mm	1.60

3.5. Model Limitations

3.5.1. Model Simplification

Inherently, a computational model is a simplification of reality, relying on necessary assumptions and abstractions. The mussel bonding model in EDEM diverges from reality in three key aspects. These factors have been incorporated into the modeling framework, which is designed to ensure sufficient predictive accuracy for the core mechanical behaviors of interest—namely, overall fracture and unloading resistance. At the material level, the real mussel shell—an anisotropic and non-uniform composite of organic matter and calcium carbonate—exhibits a complex constitutive relationship that encompasses elasticity, plasticity, and brittle fracture. The ligaments and other soft tissues are characterized as viscoelastic. In the EDEM model, inter-particle bonds are simplified as an isotropic, linear elastic-brittle material, defined by normal/tangential stiffness and strength parameters. This simplification serves as an equivalent approximation of macroscopic mechanical behavior at the particle scale. At the geometric and structural level, actual mussels possess a complex morphology with curved shells, non-uniform shell thickness, and a multi-level architecture comprising the shell, adductor muscles, and ligaments. In the EDEM model, the mussel is represented by a bonded cluster of 53 spherical particles approximating its overall shape and volume—a simplification which trades local geometric detail for the ability to capture global mechanical properties like mass distribution, moment of inertia, and force chain transmission. Regarding the failure mechanism, real mussels exhibit damage across multiple scales, encompassing brittle crack propagation within the shell, interfacial delamination

(at the organic-inorganic boundary), and the tensile or shear failure of ligaments and soft tissues. In the EDEM model, failure is modeled as the instantaneous rupture of bonds upon reaching a strength threshold. This simplification focuses on simulating the dominant 'main crack' or overall fragmentation process, rather than detailed microscopic damage mechanisms [28].

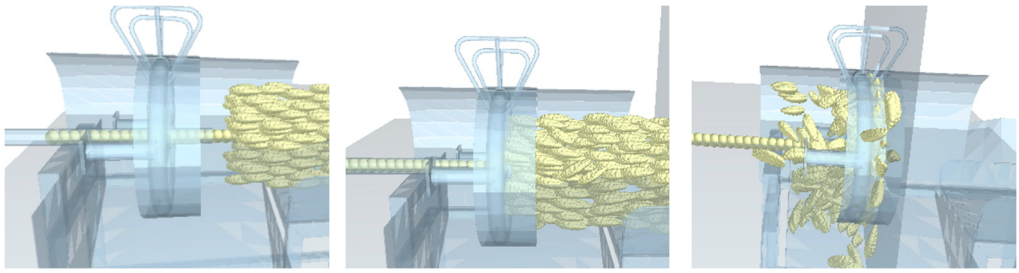
3.5.2. Model Serviceability

The EDEM model quantifies the attachment and detachment dynamics of *Mytilus coruscus* under mechanical loading, with particular focus on seedling unloading operations as a key post-harvest intervention. The applicability of this model to other mussel species requires assessment across species with differing attachment mechanics. The target species exhibits shell morphology and byssal attachment dynamics that closely mirror those of *Mytilus coruscus*, with shell lengths consistently ranging from 5 to 10 cm. This model enables robust generalization across mussel species with differing mechanical properties, as it requires only minimal parameter fine-tuning to accommodate variations in shell stiffness and byssal adhesion strength. Once calibrated, the model enables direct deployment in system optimization workflows. When applied to taxa with substantial divergence in shell stiffness and byssal adhesion strength, the model necessitates taxon-tailored parameterization and structural reconfiguration of its constitutive relationships to preserve predictive fidelity.

4. Simulation and Test Verification of Unloading Seedlings

4.1. Test Conditions

Combined with the pre-test and parameter calibration test, the physical parameters, contact parameters and Bonding V2 model parameters of mussels, seedling ropes and equipment were determined. Subsequently, the simulation test and the real test were carried out with the same diameter of the unloading hole. Observe the breaking rate of mussel particles to determine the best structural parameters. In order to improve the simulation efficiency, the three-dimensional model of the seedling unloading machine is simplified, and only the core mechanism of the seedling unloading is retained. The peeling process of mussels is shown in Figure 12: The mussel string is placed in the horizontal section of the bracket, which is transported to the front position of the peeling disc, and then peeled off through the peeling hole. A single mussel was selected for observation, and the overall force of the mussel was more than 552 N as the crushing index for statistical analysis.



(**a**) Produce material (**b**) conveying material (**c**) Stripped material

Figure 12. The simulation process of removing the mussels.

The mussels used in the prototype test were purchased from Bibo Aquaculture Service Company in Zhoushan, Zhejiang Province, with a length range of 270–310 mm and a diameter range of 18–29 mm. A total of 20 mussel strings were prepared for the experiment. One day prior to testing, they were harvested from the main cultivation ropes in the aquaculture area by boat, and then transferred to nearshore waters for temporary storage. One hour prior to testing, the mussels were collected from the shore and transported to

the experimental site. The peeling process of mussels in the field test base is shown in Figure 13. After peeling off, the damaged mussels were manually selected for statistical analysis. To ensure experimental reproducibility, all critical parameters were maintained invariant throughout the design space. Experiments were performed under controlled environmental conditions: ambient temperature of 25 ± 1 °C and relative humidity of 50 ± 5% RH. The reactor system, fabricated from 304 stainless steel, operated with a cycle duration of 20 s, driven by a 7.5 kW motor rated at 18 A.



(**a**) Place the material (**b**) conveying material (**c**) Stripped material

Figure 13. The actual process of removing the mussels.

The calculation formula of mussel damage rate B is

$$B = \frac{N_1}{N_1 + N_2} \times 100\% \quad (15)$$

In the formula, N_1—Total weight of damaged mussels
N_2—Total weight of intact mussels.

4.2. Results and Analysis

When the diameter of the unloading hole is 46 mm, 48 mm, 50 mm, 52 mm and 54 mm, respectively, the real breaking rate and the simulated breaking rate of the peeled mussel particles are shown in Figure 14.

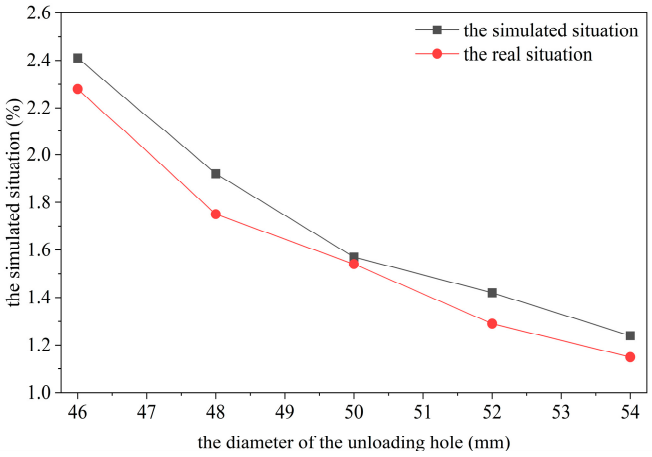


Figure 14. The degree of mussel damage under different traction forces.

The error between the simulated breaking rate of mussel particles and the real situation is 1.95–14.3%, which indicates that the parameter combination of Bonding V2 model calibrated in this paper has high accuracy. With the decrease in the diameter of the unloading hole, the damage rate of mussels gradually decreased. However, when the diameter of the unloading hole exceeded 52 mm, the damage rate of mussels decreased, but the residual mussels on the seedling rope were not completely peeled off. When the diameter of the unloading hole was 50 mm, the single root unloaded a total of 76.5 kg, of which 1.4 kg was broken.

The relevant information of screw seedling unloading equipment, drum seedling unloading equipment and this equipment is shown in Table 13. The automatic traction mussel unloader integrates the unloading process more effectively, requires less floor space, and minimizes physical damage to mussels compared to the two other equipment options. The automatic traction seedling unloader required approximately two-thirds of the operation time (per rope) compared to the drum-type equipment. The process saves approximately 11 s per cycle. In addition, it enables a reduction of one processing worker, leading to lower operational costs. The designs of both the automatic traction and screw-type seedling unloaders feature a high degree of automation. Compared with the drum-type unloader, the automatic traction system significantly reduces the physical workload for operators. The available deck space on the ship is limited, posing a significant constraint. Therefore, the automatic traction seedling unloader, which requires only about 3 m^2 of area, is recommended for its compact design. The mussel processing industry is evolving toward onboard operations, in line with current development trends. Thus, a high degree of equipment integration is a critical enabler for advancing onboard processing. The automatic traction mussel unloading equipment exhibits superiority over the two alternative systems, notably in achieving higher process integration, requiring less floor space, and inflicting lower levels of mussel damage [29].

Table 13. Summary of comparison information of the three devices.

Name of Seedling Unloading Equipment	Single Operation Time/s	Number of Processing Personnel	Automaticity	Occupied Area/m^2	Mussel Damage Rate
Automatic traction	20	2	Automatization is more excellent	3	1.2%
Screw type	20	2	Automatization is more excellent	7	3%
Drum type	31	3	Artificial rope connection and release	4	5%

The simulation and prototype show that at this time, the mussel damage rate is the lowest and the unloading effect is the best. In the experiment, the parameter setting was used to carry out the unloading test. A total of 8 tests were carried out, and the average mussel damage rate was 1.2%, which fully met the production requirements. The error comes from the adhesion of seawater on the surface of the real mussels. The seedling rope is flexible, and the bonding effect between the mussel and the seedling rope attached to the inner ring of the mussel string or the bonding effect between the mussel and the mussel after long-term use and wetting will also lead to experimental errors [30].

5. Conclusions

This study proposes an automated traction-rope mussel unloading machine, along with detailed descriptions of its overall structure and operational principles. A discrete element model of the mussel was developed based on the Bonding V2 model to simulate the mechanical interactions during the unloading process. First, uniaxial compression tests and mussel byssus bonding characteristic tests were conducted to determine the mechanical properties of mussels. The results showed an ultimate crushing displacement of 2.25 mm and an ultimate crushing load of 552 N. Additionally, the tensile force required for a single mussel foot-wire fracture ranged from 24.99 N to 58.74 N. Subsequently, the bonding parameters of the model were systematically calibrated through a three-stage optimization approach: (1) Significant factors were identified using the Plackett–Burman experimental design, (2) Parameter intervals were narrowed via the steepest ascent method, and (3) the optimal parameter combination was determined by the Box–Behnken response surface methodology. Using the Design-Expert optimization tool, the following calibrated

parameters were determined: normal stiffness per unit area (2.48×10^{11} N/m^3), tangential stiffness per unit area (3.80×10^8 N/m^3), critical normal stress (3.15×10^6 Pa), critical tangential stress (2.90×10^7 Pa), and the contact radius (1.60 mm). The performance of the mussel unloading machine was evaluated through EDEM simulations and physical validation tests. Key structural parameters were optimized, including an unloading hole diameter of 50 mm. At the microscale, the DEM reveals the mechanistic consistency of the optimized parameters with observed particle interactions; at the macroscale, prototype testing confirms the model's predictive fidelity in reproducing system-level performance. The dual validation of model predictions against physical measurements not only establishes the reliability of the optimization framework but also precisely delimits its operational boundaries across heterogeneous system states. Under these optimized parameter conditions, experimental results demonstrated an average mussel damage rate of only 1.2%, confirming the high accuracy of the calibrated Bonding model parameters proposed in this study.

While this study elucidated the role of the circular aperture in mussel damage under controlled conditions, its generalizability to other shellfish taxa remains to be characterized, as key operational parameters—including traction speed and support frame inclination—were not systematically evaluated. By automating manual handling and minimizing product loss, the system achieves significant cost-effectiveness, enabling scalable deployment without proportional increases in labor input. To enable large-scale deployment, future work should prioritize enhancing equipment durability for continuous operation and developing standardized interfaces with automated sorting and transportation systems. The design principle establishes a robust foundation for large-scale deployment, but its long-term reliability under extreme conditions warrants validation through pilot-scale trials.

Author Contributions: Conceptualization, Z.L. and H.Y.; methodology, H.Y. and C.L.; software, X.L.; validation, Z.L., H.Y. and X.L.; formal analysis, X.L. and C.L.; investigation, X.L.; resources, Z.L. and H.Y.; writing—original draft preparation, X.L.; writing—review and editing, Z.L., H.Y. and C.L. All authors have read and agreed to the published version of the manuscript.

Funding: Agricultural "Double Strengthening" Key Breakthrough Projects (Grant No. 21047007323).

Data Availability Statement: Data will be made available upon request.

Conflicts of Interest: The authors declare no conflict of interest.

References

1. Gao, W.; Wang, Z.; Zhang, S.; Lin, J.; Tan, Y.; Li, X.; Chen, J. Characteristics of fish assemblage in a mussel farming area in Gouqi Island waters. *J. Fish. China* **2024**, *48*, 52–67.
2. Luo, H.; Tao, L.; Wu, Y.; Zhang, X.; Yang, D. Thoughts on sustainable development of mussel industry in Shengsi County, Zhejiang Province. *China Fish.* **2016**, *12*, 29–33.
3. Murchie, L.W.; Cruz, R.M.; Kerry, J.P.; Linton, M.; Patterson, M.F.; Smiddy, M.; Kelly, A.L. High pressure processing of shellfish: A review of microbiological and other quality aspects. *Innov. Food Sci. Emerg. Technol.* **2005**, *6*, 257–270. [CrossRef]
4. Li, X.; Wang, T. Safety monitoring of bivalves in Europe. *China Fish.* **2005**, *4*, 15–17.
5. Alfaro, A.C.; Jeffs, A.G. Variability in mussel settlement on suspended ropes placed at Ahipara Bay, Northland, New Zealand. *Aquaculture* **2003**, *216*, 115–126. [CrossRef]
6. Luo, Z.; Zhou, Z.; Fu, Z.; Jia, S. Design and Research of Mussel Harvesting Device. *China Water Transp.* **2018**, *18*, 109–110.
7. Cheng, H.; Yuan, Y.; Li, D. Design and Research of Double-station Chain Mussel Unloading Equipment. *Mech. Eng.* **2019**, *12*, 62–65.
8. Cheng, H.; Yuan, Y.; Xie, F.; Li, D. Design of Screw-Driving Mussel Breeding Rope Removal Equipment. *Light Ind. Mach.* **2021**, *39*, 23–28+34.
9. Jiang, C. Major problems and solutions of shellfish processing in China. *Fish. Inf. Strategy* **2012**, *27*, 87–93. [CrossRef]
10. Liu, C. Structure Optimization of Vertical Iron Roller Rice Mill Based on Discrete Element EDEM. Master's Thesis, Wuhan Polytechnic University, Wuhan, China, 2024.

11. Shi, J.; Shan, Z.; Yang, H. Research on the macro- and meso-mechanical properties of frozen sand mold based on Hertz-Mindlin with Bonding model. *Particuology* **2024**, *88*, 176–191. [CrossRef]
12. Zhou, J.; Zhang, L.; Hu, C.; Li, Z.; Tang, J.; Mao, K.; Wang, X. Calibration of wet sand and gravel particles based on JKR contact model. *Powder Technol.* **2022**, *397*, 117005. [CrossRef]
13. Li, S.; Diao, P.; Miao, H.; Zhao, Y.; Li, X.; Zhao, H. Modeling the fracture process of wheat straw using a discrete element approach. *Powder Technol.* **2024**, *439*, 119726. [CrossRef]
14. Li, H.; Meng, Y.; Qi, X. Discrete Element Modelling Method and Parameter Calibration of Garlic Species Based on Bonding V2 Model. *Trans. Chin. Soc. Agric. Mach.* **2025**, *56*, 150–157+169.
15. Yuan, Y.; Xie, F.; Fan, Q. Pressure Bearing Properties and Crack Path Orientation of Mussel Shell. *Agric. Eng.* **2022**, *12*, 63–67. [CrossRef]
16. Xu, W.; Xie, Y.; Qian, J. Adhesive Performance of 3D Printed Biomimetic Mussel Byssal Structures. *Appl. Math. Mech.* **2024**, *45*, 261–272.
17. Knysh, A.; Tsukrov, I.; Chambers, M.; Swift, M.R.; Sullivan, C.; Drach, A. Numerical modeling of submerged mussel longlines with protective sleeves. *Aquac. Eng.* **2020**, *88*, 102027. [CrossRef]
18. Zhang, P.; Li, F.; Wang, F. Optimization and test of ginger-shaking and harvesting device based on EDEM software. *Comput. Electron. Agric.* **2023**, *213*, 108257. [CrossRef]
19. Yin, Q.; Xia, X.; Liu, X.; Zhang, Y.; Song, S.; Li, H. Structural optimization design of spiral-driven grain detection robot based on EDEM-RecurDyn. *Smart Agric. Technol.* **2025**, 101182. [CrossRef]
20. Li, H.; Zhang, G.; Liu, F.; Li, X.; Wang, Y.; Mu, G. Design and Testing of Mudflat Shellfish Vibrating Harvester Based on DEM-MBD Simulation. *Trans. Chin. Soc. Agric. Mach.* **2024**, *55*, 361–370.
21. Xie, F. Study on Key Technology of Mussel High-Pressure Water Jet Cleaning. Master's Thesis, Zhejiang Ocean University, Zhoushan, China, 2024.
22. Sunny, R.C.; Fredriksson, D.W.; Tsukrov, I.; Zhu, L.; Bowden, M.; Chambers, M.; Silkes, B. Design considerations for a continuous mussel farm in New England Offshore waters. Part II: Using validated numerical models to estimate the probability of failure. *Aquac. Eng.* **2025**, *111*, 102575. [CrossRef]
23. Huang, W. Design and Experimental Study of Centrifugal Shellfish Seeding Device. Master's Thesis, Dalian Ocean University, Dalian, China, 2022.
24. Yang, W. Investigation on the Mechanical Properties of Saxidomus Purpuratus Shells. Doctor's Thesis, Northeastern University, Boston, MA, USA, 2012.
25. Kan, Y. Investigation on Adhesion Mechanisms of Mussel Foot Proteins Using the Surface Forces Apparatus. Doctor's Thesis, Southest University, Dhaka, Bangladesh, 2016.
26. Zeng, D.; Yang, H.; Zeng, Z.; Liu, H.; Du, Z. Parameter Sensitivity Study of Dynamic Response of Simply Supported Girder Bridge Under Main Aftershock. *Railw. Eng.* **2025**, *65*, 75–82.
27. Du, G.; Zhang, H.; Yu, H.; Hou, P.; He, J.; Cao, S.; Wang, G.; Ma, L. Study on Automatic Tracking System of Microwave Deicing Device for Railway Contact Wire. *IEEE Trans. Instrum. Meas.* **2024**, *73*, 3527611. [CrossRef]
28. Jia, X.; Zheng, X.; Chen, L.; Liu, C.; Song, J.; Zhu, C.; Xu, J.; Hao, S. Discrete element flexible modeling and experimental verification of rice blanket seedling root blanket. *Comput. Electron. Agric.* **2025**, *233*, 110155. [CrossRef]
29. Cheng, H. Development of a New Type of Thick-Shell Mussel Scrubbing Equipment. Master's Thesis, Zhejiang Ocean University, Zhoushan, China, 2022. [CrossRef]
30. Wang, Q.; Chen, Z.; Huang, H.; Huang, G.; Zeng, Z.; Yang, B. Design and Test of Mower Cutting System Parameters Based on EDEM. *China South. Agric. Mach.* **2025**, *56*, 7–13.

Disclaimer/Publisher's Note: The statements, opinions and data contained in all publications are solely those of the individual author(s) and contributor(s) and not of MDPI and/or the editor(s). MDPI and/or the editor(s) disclaim responsibility for any injury to people or property resulting from any ideas, methods, instructions or products referred to in the content.